THE JOURNAL OF PHYSICAL CHEMISTRY B

Article

Cite This: J. Phys. Chem. B 2018, 122, 11626−11639

pubs.acs.org/JPCB

Dispersion Correction Alleviates Dye Stacking of Single-Stranded DNA and RNA in Simulations of Single-Molecule Fluorescence Experiments

Kara K. Grotz,[†] Mark F. Nueesch,[‡] Erik D. Holmstrom,[‡] Marcel Heinz,[†] Lukas S. Stelzl,[†] Benjamin Schuler,*[,‡,¶] and Gerhard Hummer*[,†,§]

[†]Department of Theoretical Biophysics, Max Planck Institute of Biophysics, 60438 Frankfurt am Main, Germany

[‡]Department of Biochemistry, University of Zurich, 8057 Zurich, Switzerland

[¶]Department of Physics, University of Zurich, 8057 Zurich, Switzerland

[§]Institute of Biophysics, Goethe University Frankfurt, 60438 Frankfurt am Main, Germany

Supporting Information

ABSTRACT: We combine single-molecule Förster resonance energy transfer (single-molecule FRET) experiments with extensive all-atom molecular dynamics (MD) simulations (>100 μs) to characterize the conformational ensembles of single-stranded (ss) DNA and RNA in solution. From MD simulations with explicit dyes attached to single-stranded nucleic acids via flexible linkers, we calculate FRET efficiencies and fluorescence anisotropy decays. We find that dispersion-corrected water models alleviate the problem of overly abundant interactions between fluorescent dyes and the aromatic ring systems of nucleobases. To model dye motions in a computationally efficient and conformationally exhaustive manner, we introduce a dye-conformer library, built from simulations of dinucleotides with covalently attached dye molecules. We use this library to calculate FRET efficiencies for dT_{19}, dA_{19}, and rA_{19} simulated without explicit labels over a wide range of salt concentrations. For end-labeled homopolymeric pyrimidine ssDNA, MD simulations with the parmBSC1 force field capture the overall trend in salt-dependence of single-molecule FRET based distance measurements. For homopolymeric purine ssRNA and ssDNA, the DESRES and parmBSC1 force fields, respectively, provide useful starting points, even though our comparison also identifies clear deviations from experiment.

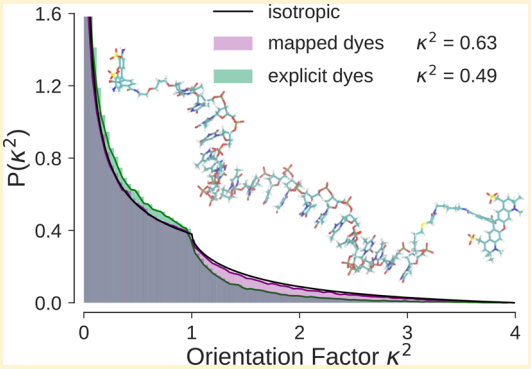

INTRODUCTION

Single-stranded nucleic acids (ssNAs) lie at the heart of the biological information flow from DNA to RNA to protein. Single-stranded DNA (ssDNA) forms, e.g., during transcription, at telomeric overlaps, at DNA double-strand breaks, and at replication forks.[1,2] Single-stranded RNA (ssRNA) plays fundamental roles in transcription and translation, and in the regulation of these processes, e.g., through riboswitches[3,4] or regulating mRNA degradation.[5,6] In biotechnology and molecular medicine, ssRNA is used, e.g., to construct aptamers for biotechnological and biomedical sensing[7] or as microRNA to regulate gene expression.[8]

Despite these crucial roles and possible applications of ssNAs, conformational dimensions and dynamics of unstructured stretches remain relatively poorly understood compared to the well-characterized helical double-stranded or folded nucleic acids. The reason is that obtaining atomic resolution structures of short and flexible ssNAs is very challenging.[9−12] Pulling experiments such as single-molecule atomic force microscopy (AFM) are capable of providing mechanical data, e.g., on the stability of base-stacking interactions.[13] AFM experiments, however, provide only limited information on the molecular conformations.[14] Small-angle X-ray scattering (SAXS) experiments provide information on the global shape and size of ssNAs.[15] Pollack and co-workers recently managed to describe SAXS data of the single-stranded homopolymers dT_{30}/dT_{40} and dA_{30}/dA_{40} by optimizing an ensemble of predefined structures.[9,10] However, typical SAXS experiments do not yield dynamics directly. Nuclear magnetic resonance (NMR) measurements yield high-resolution dynamical and structural information on, e.g., short fragments[11,16,17] and large structured RNAs,[18,19] but high-resolution studies on ∼20 nucleotide long unstructured ssNAs are challenging.[20]

Förster resonance energy transfer (FRET) measurements provide a powerful alternative to characterize flexible molecular

Special Issue: William A. Eaton Festschrift

Received: August 6, 2018
Revised: October 2, 2018
Published: October 4, 2018

DOI: 10.1021/acs.jpcb.8b07537
J. Phys. Chem. B 2018, 122, 11626−11639

systems. FRET reports on both dynamics and distances between fluorescence dyes attached to flexible polymers like ssNAs.[15,21,22] As a "spectroscopic ruler," FRET probes distances on biomolecular length scales.[23] Single-molecule FRET has the advantages of avoiding ensemble averaging within the experiments[24−26] and of resolving dynamics, e.g., of the transition path time in the folding of nucleic-acid hairpins.[27]

The combination of single-molecule FRET experiments with molecular dynamics (MD) simulations aims to overcome the main intrinsic problem of FRET methods, namely not being able to directly resolve three-dimensional structures.[22,28−36] MD simulations describe the conformational dynamics of ssNAs at atomic resolution, albeit on the basis of approximate classical potential energy functions. Eaton and co-workers[29] demonstrated the power of combining single-molecule FRET experiments and simulations in their studies of protein dynamics in the unfolded state. Comparing the results of these two approaches not only affords the possibility to interpret single-molecule FRET experiments in more detail, but also provides an opportunity to test simulations and the underlying force fields, i.e., the potential energy functions describing the interactions in MD simulations. For DNA, two recent force fields, OL15[37] and parmBSC1,[38] describe DNA double helices with high accuracy[39−41] and also hold great promise for single-stranded DNA.[38] The description of RNA, however, is very challenging[12,42] and simulations of hairpins and tetranucleotides[43] revealed force field deficiencies. Recently, a new RNA force field was developed by Shaw and co-workers, which improved the agreement with NMR measurements of tetranucleotides.[44]

Despite these advanced MD force fields, comparisons between single-molecule FRET and MD remain challenging, partly due to the presence of the donor and acceptor fluorophores.[22,28−36] Proteins and double-stranded DNA have been simulated with dyes attached,[45] albeit often with only repulsive dye−macromolecule interactions to sample the sterically accessible space.[29,30] When attractive interactions were included, water−protein and water−dye interactions had to be scaled to prevent the dye from stacking onto the protein.[22,36,46] For nucleic acids, this stacking problem of the dyes is expected to be even more severe. Overly strong interactions between the extended aromatic ring systems may overstabilize configurations where the dye is stacked against nucleobases.[47]

For a direct and quantitative comparison of FRET experiments and MD simulations, an explicit description of the dyes in the simulations is critical. Here we aim to overcome the stacking problem by employing the TIP4P-D[48] and TIP4P/2005(1.1)[46,49] water models that introduce corrections for water−water and water−solute London dispersion interactions, respectively. The dispersion corrections lead to an increased solvation of the dyes and thus to a reduction of their artificial stacking to adjacent nucleobases. With an improved description of the dyes at hand, we demonstrate that MD simulations of ssRNA can roughly reproduce the dimensions observed in single-molecule FRET experiments, and that simulations of ssDNA capture the overall trend in salt-sensitivity established experimentally. Even though our comparison shows clear deviations from experiment, it can serve as a starting point toward quantitative characterization of ssNAs.

METHODS AND MATERIALS

Parametrization of the Fluorescent Dyes. One of the aims of this study is to compare the simulated distances between the fluorophores, and thus the simulated FRET efficiencies, directly to experiment. Therefore, we require a realistic description of the fluorescent dyes, Alexa Fluor 594 and Alexa Fluor 488 (in the following Alexa 594 and 488), which were used as fluorescence acceptor and donor, respectively, and their linkers (Figure 1). A maleimide

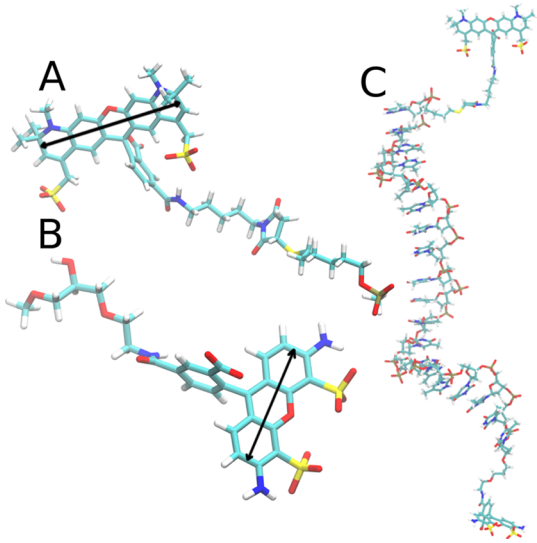

Figure 1. Fluorescent dyes and ssDNA with dyes. (A) Alexa 594 and (B) Alexa 488 including methyl-capped linkers. Arrows indicate the transition dipole moment vectors $\boldsymbol{\mu}$. (C) Single-stranded homopolymeric dT_{19} with Alexa 594 attached at the 5′ end and Alexa 488 attached at the 3′ end.

functionalized Alexa 594 is covalently coupled to a thiol linker attached to the 5′ end of the nucleic acids. A *N*-hydroxysuccinimide (NHS) ester functionalized Alexa 488 is coupled to an amino linker attached to the 3′ end of the nucleic acid. The Alexa 594 and 488 dyes are available as a mixture of 5- and 6-isomers. Only the 5-isomers were used in simulations, since only a minor dependence of the choice of the isomer on the calculated average properties is expected.[50] All carboxylate and sulfate groups were assumed to be deprotonated. The dyes, their linkers, and a capping methyl group were denovo parametrized using the automated atom type and bond type perception of Antechamber[51] to obtain a GAFF force field.[52,53] RESP partial charges were obtained at the HF/6-31G* level of theory in vacuum for methyl-capped dyes. The partial charges of the cap were uniformly distributed over the whole residue, and the resulting charges adjusted slightly to give an integer net charge. The charges are listed in Table S1 (Alexa 594) and Table S2 (Alexa 488) in the Supporting Information.

Dye Dynamics Employing Different Water Models. The performance of both newly parametrized dyes was evaluated in MD simulations with five water models (TIP3P,[54] TIP4P-Ew,[55] TIP4P/2005,[49] TIP4P/2005(1.1),[46,49] and TIP4P-D[48]) using thymine dinucleotides with single dyes attached. Besides the standard TIP3P model, we tested the TIP4P-Ew water model, as this has been reported to stabilize the unfolded state for proteins and may also help to better solvate disordered nucleic acids.[56] In the

DOI: 10.1021/acs.jpcb.8b07537
J. Phys. Chem. B 2018, 122, 11626−11639

TIP4P/2005(1.1) setup, the strength of the Lennard-Jones interaction parameter ϵ between the attached dye and water was scaled by a factor of 1.1. In this way, the interaction of the dye with water is slightly more favored compared to TIP4P/2005. The TIP4P-D model contains a correction for underestimated London dispersion forces and thus leads to increased solvation of the dinucleotide. These 10 minimal systems were simulated for 500 ns at 150 mM NaCl concentration using the same simulation conditions as for the unlabeled 19mer nucleic acid simulations introduced below. The simulations were run in small cubic boxes with an edge length of 5 nm, resulting in simulation systems with around 29 000 atoms.

Simulations of Unlabeled ssDNA and ssRNA. We simulated unlabeled homopolymeric 19mer deoxythyminemonophosphate (dT_{19}), deoxyadenosinemonophosphate (dA_{19}), and adenosinemonophosphate (rA_{19}). The simulations were initiated from single-stranded helical starting structures built with the Nucleic Acid Builder.[57] Each of the nucleic acids was solvated in a cubic box with an edge length of 8.5 nm, resulting in systems with approximately 65 000 atoms. For unlabeled DNA, the parmBSC1[38] force field and TIP3P water[54] were used. For unlabeled RNA modeled with the parmBSC0χ_{OL3}[58−60] force field, TIP3P,[54] TIP4P/2005(1.1)[46,49] (here scaling the interaction of water with the nucleic acid), or TIP4P-D water[48] were used. For unlabeled RNA modeled with the DESRES[44] force field, TIP4P-D water was used. Simulations were conducted at 15 mM, 150 mM, and 845 mM NaCl using ion parameters by Joung and Cheatham.[61] All DNA and RNA simulation setups employing parmBSC0χ_{OL3} were prepared using the tLEaP module.[57] AMBER simulation systems were converted for GROMACS[62] simulations using ACPYPE.[63] The RNA systems using the DESRES force field[44] were built directly with GROMACS.[62]

Unbiased MD simulations were performed with GROMACS[62] (v. 4.6.7, v. 5.1.3, v. 2018). Energy minimization was followed by equilibration simulations of 2 ns. P-LINCS[64] was used to constrain bonds involving hydrogen atoms to their equilibrium lengths, enabling a time step of 2 fs. The pressure was kept at 1 atm with the Berendsen barostat[65] (τ_p = 1.0 ps) in order to efficiently relax the box size during the equilibration phase. Using the velocity-rescale thermostat by Bussi et al.,[66] the temperature was kept at 300 K. Real-space van der Waals and electrostatic interactions were truncated at 1 nm. Long-range electrostatics were computed using the particle mesh Ewald method[67] with a Fourier spacing of 0.16 nm and in a second set of simulations of 0.12 nm. Random velocities were drawn from a Maxwell−Boltzmann distribution.

The equilibration was followed by a production run under the same conditions as the equilibration but using the Parrinello−Rahman barostat[68] (τ_p = 4.0 ps). Trajectories of approximately 20 μs were obtained for each DNA system, 120 μs in total. The RNA using the parmBSC0χ_{OL3} force field[58−60] was simulated for 12, 0.7, and 3 μs, solvated in the water models TIP3P,[54] TIP4P/2005(1.1)[46,49] and TIP4P-D,[48] respectively, at each salt concentration. For the RNA with the DESRES force field[44] multiple trajectories of about 7 μs in total were created for each salt condition. The first 4 ns of the trajectories were excluded from the analysis in all systems to extend the equilibration phase. The trajectory analysis (including, e.g., calculation of correlation functions or computation of orientation factors, FRET efficiencies, distance time traces, and distributions, etc.) was performed using Python (v. 2.7, available at www.python.org), and the MDAnalysis (v. 0.17.0)[69,70] and MDTraj (v. 1.8.0)[71] packages. Trajectories were visualized with VMD (v. 1.9.1−3).[72]

ssDNA Simulations with Fluorescent Dyes Covalently Attached. We used the TIP4P-D[48] and the TIP4P/2005(1.1)[46,49] water models to study the orientation and dynamics of dyes attached to ssDNA. In the TIP4P/2005(1.1) setup, the nonelectrostatic interactions of the dyes with water were scaled by a factor of 1.1. The dyes were attached to the two ssDNA chains (A594-Mal-5′-dX_{19}-3′-NHS-A488, X = T, A) and simulated for 2 and 4 μs (dT_{19} and dA_{19}, respectively) in a simulation box with an edge length of 12 nm containing about 230 000 atoms, under the same simulation conditions as for unlabeled NAs.

Conformational Libraries. Singly labeled dinucleotides were simulated to generate a library of dye conformations. Both dT_2 and dA_2 were labeled first with Alexa 594 at the 5′ end and then, in a second round of simulations, with Alexa 488 at the 3′ end (A594-Mal-5′-dX_2 and dX_2-3′-NHS-A488, X = T, A). With these dinucleotides, we aim to capture the chemistry of the respective nucleic acid termini while minimally restricting the motion of the attached dyes to ensure good coverage of sterically possible configurations. The labeled dinucleotides were solvated with the TIP4P-D water model[48] and simulated using the same simulation conditions as for the unlabeled 19mer nucleic acid simulations described above. The simulations were run in small cubic boxes with an edge length of 5 nm, resulting in simulation systems with around 29 000 atoms. For each setup, simulations were run at low, intermediate, and high salt concentrations (15 mM, 150 mM, and 845 mM NaCl). From each of these 500 ns long trajectories, 25 000 snapshots were taken and saved as individual structures to build a conformational library.

Mapping Procedure. To capture the conformational and dynamical characteristics of the dyes, a mapping approach was developed. Rotamer libraries are commonly used to model electron paramagnetic resonance experiments.[32,33,73] In case of FRET,[74] the mapping approach is motivated by the fast orientational relaxation of the fluorescent dyes seen in fluorescence anisotropy decay measurements. From a dye conformational library (see previous section), snapshots of dye conformations were chosen randomly and mapped onto the structures along trajectories of long unlabeled 19mer ssDNA and ssRNA, separated by a time interval of 0.2 ns. In this way, our mapping approach mimicked the fast dynamics of the dyes observed in the FAD measurements. We implemented the mapping algorithm in Python using the MDAnalysis package[69,70] to model dye configurations that do not clash with the nucleic acids. The nucleobase coordinates from the conformational library of the respective dye and its adjacent nucleotide (dT for dT_{19}; dA for dA_{19} and rA_{19}) were aligned to the last terminal residue at each end of the unlabeled ssDNAs and ssRNAs to generate candidate dye conformations. Dye conformers were excluded if any of their heavy atoms was within 3.7 Å of the heavy atoms of the nucleic acid. For each nucleic acid configuration we tried up to 12 000 randomly chosen pairs of dye configurations, one at each end. If no matching dye configuration could be found (e.g., because the 5′ and 3′ ends were in close proximity), the respective ssNA configuration was excluded from further analysis because of its steric inaccessibility in the dye-labeled state. For simplicity, all other configurations were given equal weight. Instead of using a hard cutoff, we could have used a smooth function to

DOI: 10.1021/acs.jpcb.8b07537
J. Phys. Chem. B 2018, 122, 11626−11639

describe the overlap between nucleic acids and the dyes and reweighted each simulation structure accordingly. The total length of the trajectories is hence reduced from ∼120 to ∼110 μs for ssDNA and from ∼21 to ∼18 μs for ssRNA.

FRET Efficiencies from MD Simulations. For simulations of NAs with dyes attached, the path integral according to Makarov and Plaxco[75] was employed to calculate the mean FRET efficiency

$$\langle E \rangle = 1 - k_D \int_0^\infty I(t)\, \mathrm{d}t \tag{1}$$

where $\tau_D = {k_D}^{-1}$ is the experimentally determined fluorescence lifetime of the donor in the absence of an acceptor (∼4 ns for Alexa 488 and of Alexa 594, see Methods). The normalized decay in donor fluorescence intensity $I(t)$ was calculated as

$$I(t) = \left\langle \mathrm{e}^{-\int_0^t [k_D + k_T(R(t'))]\, \mathrm{d}t'} \right\rangle \tag{2}$$

where the average $\langle \cdots \rangle$ is over starting points along the trajectories. The integral in eq 1 was truncated at t_{max} = 20 ns $\simeq 5\tau_D$. In case of the mapped dye conformations, an additional average was performed over dye orientations drawn at random from the library. According to Förster theory,[76] the transfer rate $k_T(R)$ is given by

$$k_T(R) = \frac{3}{2}\kappa^2 k_D \left(\frac{R_0}{R}\right)^6 \tag{3}$$

where R is the interdye distance, κ^2 is the orientation factor defined as

$$\kappa^2 = [\hat{\boldsymbol{\mu}}_D \cdot \hat{\boldsymbol{\mu}}_A - 3(\hat{\mathbf{R}} \cdot \hat{\boldsymbol{\mu}}_A)(\hat{\mathbf{R}} \cdot \hat{\boldsymbol{\mu}}_D)]^2 \tag{4}$$

and R_0 is the Förster radius for isotropic dye orientations where $\kappa^2 = 2/3$. $\mathbf{R}$ is the vector from one dye center to the other, with R its length, and $\hat{\mathbf{R}}$ the corresponding unit vector. $\hat{\boldsymbol{\mu}}_D$ and $\hat{\boldsymbol{\mu}}_A$ are the unit vectors in the direction of the transition dipole moments of donor and acceptor, respectively (Figure 1). For the probability density and models of the dynamics of κ^2, see ref 77.

For the evaluation of eq 2, time-continuous trajectories are required. In case of dye mapping, we considered uninterrupted MD-trajectory segments of at least 100 ns in length. The FRET efficiency (eq 1) was calculated individually for each of these segments. These individual efficiency values were weighted according to the length of their respective trajectory segment (number of frames) to give an estimate of the mean FRET efficiency for the given condition. Block averaging was used to estimate standard errors of the means.

Fluorescence Anisotropy from MD Simulations. The dynamics of the fluorescent dyes from simulation can be compared to measurements of the fluorescence anisotropy decay (FAD). The anisotropy is evaluated from the decay of the correlation function

$$r(t) = r_0 \langle P_2(\hat{\boldsymbol{\mu}}(t) \cdot \hat{\boldsymbol{\mu}}(0)) \rangle \tag{5}$$

where $P_2(x) = (3x^2 - 1)/2$ is the second-order Legendre polynominal with $\hat{\boldsymbol{\mu}}(t)$ being the unit vector in the direction of the transition dipole moment of the respective dye (Figure 1). For the fundamental anisotropy r_0, the limiting anisotropy of 0.38 determined experimentally for Alexa 594 and 488[78] was used instead of the theoretical value of 2/5.

For FAD analysis, we adopted the model-free approach developed by Lipari and Szabo for NMR relaxation experiments,[79] in a form extended to multiple time scales.[80] The autocorrelation function $r_I(t)$ of the orientational motion of just the dyes and linkers (i.e., for $r(t)$ evaluated in the fixed reference frame of the ssNAs) captures the "internal motion," which we described by

$$r_I(t) = S^2 + (1 - {S_f}^2)\mathrm{e}^{-t/\tau_f} + ({S_f}^2 - S^2)\mathrm{e}^{-t/\tau_s} \tag{6}$$

where S^2 is the generalized order parameter, a model independent measure of the degree of spatial restriction, defined as $S^2 = r_I(t \to \infty)$. ${S_f}^2$ is the generalized order parameter for just the fast motion of the dye. Smaller values of ${S_f}^2$ indicate less restriction in the fast dye motions and thus less prominent interactions with nucleobases.

Single-Molecule FRET Sample Preparation and Measurements. *Labeling.* Fluorescently labeled samples of the ssNA variants were obtained by covalently linking Alexa 488 via NHS-ester chemistry to a primary amino group at the 3′ end and Alexa 594 via maleimide chemistry to the thiol group at the 5′ end of the orthogonally functionalized oligonucleotides. Prior to use, doubly and singly labeled oligonucleotides were purified using high-pressure liquid-chromatography (HPLC) and a reverse-phase HPLC column (Dr. Maisch, Reprosil Pur 200-C18 AQ).

Single-Molecule FRET Measurements. Single-molecule data of fluorescently labeled oligonucleotides freely diffusing in solution were measured on a MicroTime 200 system from PicoQuant equipped with two pulsed interleaved excitation lasers (pulse repetition rate of 20 MHz each). The donor was excited with a 485 nm diode laser (LDH DC 485) and the acceptor was excited with a pulsed super continuum laser (SuperK EXTREME EXW 12) using a band-pass filter (Z582/15) to select the desired wavelength. The average laser powers were set to 100 μW and 45 μW, respectively (measured at the back aperture of the objective). Each sample (50−100 pM) was measured at 22 °C in 10 mM HEPES buffer (3.47 mM NaOH, pH 7.0), 0.001% Tween 20, 0.143 M β-mercaptoethanol (BME), and NaCl concentration as specified.

Data Analysis. The data were analyzed using Wolfram Mathematica 11.3 software combined with custom-developed C++ code (by Dr. D. Nettels). The trajectories were divided into time bins of lengths equal to the corresponding mean diffusion times observed at each experimental condition. Bursts of photons were selected using a search algorithm which defines a burst as a time bin of 0.5−0.7 ms with more than 25 photons after either donor or acceptor excitation. The numbers of photons in each burst were corrected for background, the different detection efficiencies of the donor and acceptor fluorophores, crosstalk and acceptor direct excitation, as described by Kapanidis et al.[81,82] Correction factors for all ssNA variants were obtained from the measurement of the singly and doubly labeled variant of dT_{19}, which shows stable lifetimes (∼4 ns for both Alexa 594 and 488) under all experimental conditions. The transfer efficiency E of each burst was calculated using the corrected number of the donor, n_D, and acceptor, n_A, photons after donor excitation,

$$E = \frac{n_A}{n_A + n_D} \tag{7}$$

E values from all bursts within a single measurement were used to construct a transfer efficiency histogram. The mean transfer efficiency, $\langle E \rangle$, of the doubly labeled species at every

DOI: 10.1021/acs.jpcb.8b07537
J. Phys. Chem. B 2018, 122, 11626−11639

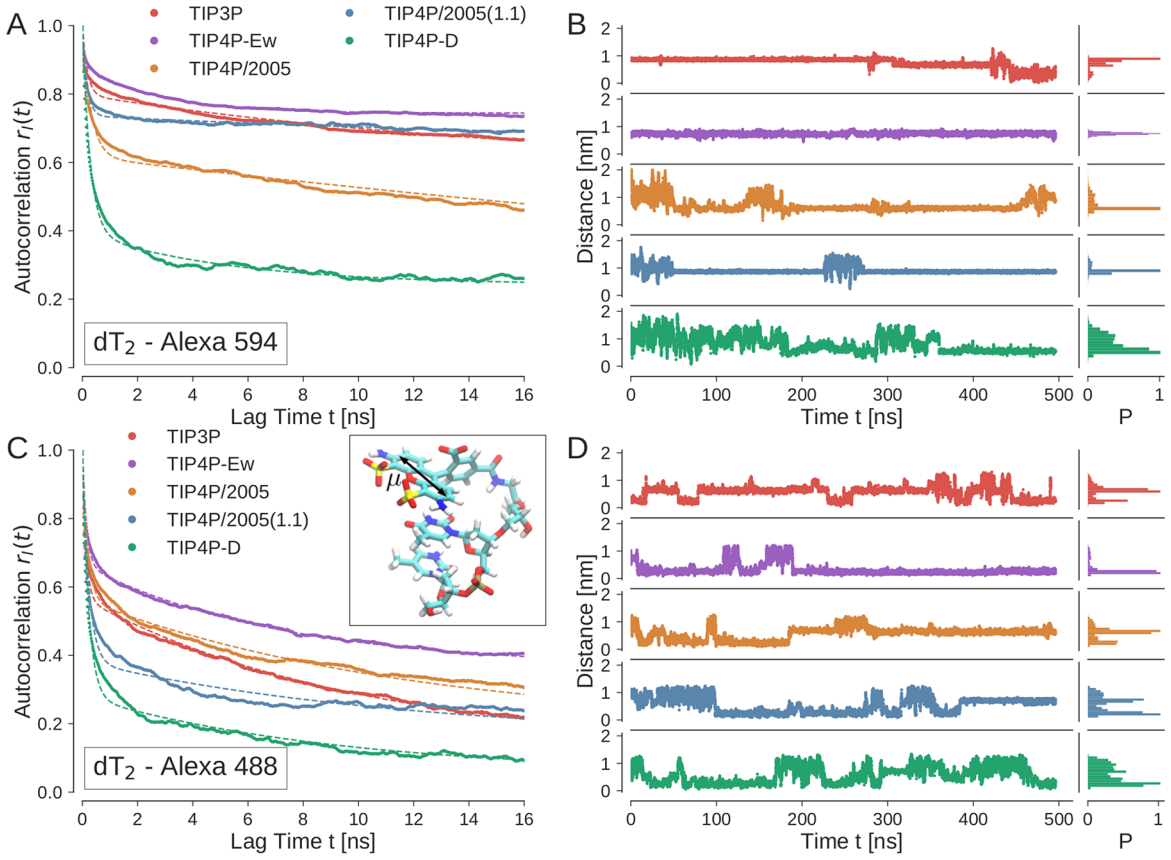

Figure 2. Dye rotational dynamics. (A, C) FAD correlation functions $r_l(t)$ (solid lines) of fluorescent dyes Alexa 594 (A) and Alexa 488 (C) attached to thymine-dinucleotide from MD simulations at intermediate salt concentration (150 mM NaCl) with different water models (solid lines). The decay curves were fitted according to the model-free approach[79,80] in eq 6 (dashed lines; fit parameters in Table 1). Dinucleotides were aligned by optimal superposition to fix the reference frame and to remove overall tumbling. (B, D) Time traces of the distances between the geometric center of the central ring of the dye and the geometric center of its directly adjacent nucleobase for Alexa 594 (B) and Alexa 488 (D). The plots on the right show the distance distributions, scaled to unit maximum.

experimental condition was obtained by fitting with a Gaussian peak function (see Figure S3 in the Supporting Information).

Interdye Distance Calculation. To infer interdye distances from transfer efficiency measurements of conformationally heterogeneous polymers such as ssNAs, one needs to have a suitable model for the underlying distance probability density function, $P(R)$. Given a model for $P(R)$, the mean transfer efficiency can be obtained from eq 8 provided that (1) the rotational correlation times of the fluorophores are short relative to the fluorescence lifetime of the donor in the presence of the acceptor, τ_{DA}, and (2) the donor−acceptor distance fluctuations are slow relative to τ_{DA}.[25] We then have

$$\langle E \rangle = \int_0^{l_c} P(R)E(R)\,\mathrm{d}R \tag{8}$$

with $E(R) = [1 + (R/R_0)^6]^{-1}$. Here, $l_c = 19.1$ nm is the contour length of the labeled oligonucleotides measured from the central oxygen of Alexa 488 to the central oxygen of Alexa 594 and $R_0 = 5.4$ nm is the Förster radius associated with the two dyes.

Semiflexible polymer models have been widely used to describe fluorescence experiments on nucleic acids in solution.[83] We used the end-to-end distance distribution of the worm-like chain (WLC) model,[84]

$$P_{\mathrm{WLC}}(R, l_p, l_c) = \frac{4\pi(R/l_c)^2}{Cl_c(1 - (R/l_c)^2]^{9/2}} \mathrm{e}^{-3l_c/4l_p[(1-(R/l_c)^2)} \tag{9}$$

with

$$C = \pi^{2/3}\mathrm{e}^{-\alpha}\alpha^{-3/2}\left(1 + \frac{3}{\alpha} + \frac{15}{4\alpha^2}\right) \tag{10}$$

and $\alpha = 3l_c/4l_p$. The persistence length l_p depends on ionic strength,[15] which affects $P_{\mathrm{WLC}}(R, l_p, l_c)$ and in turn modulates the mean transfer efficiency. Using our experimentally determined value of $\langle E \rangle$ and eq 9, we solved eq 8 numerically to obtain l_p, which we then used together with l_c to calculate mean interdye distances as $\langle R \rangle = \int_0^{l_c} RP_{\mathrm{WLC}}(R, l_p, l_c)\,\mathrm{d}R$.

As a simple but coarse alternative, we considered a truncated normal distribution, defined for positive distances R,

$$P_{\mathrm{norm}}(R, \mu, \sigma) = C^{-1}\mathrm{e}^{-(\mu-R)^2/2\sigma^2} \text{ for } R > 0 \tag{11}$$

with $C = (\pi/2)^{1/2}\sigma[1 + \mathrm{erf}(\mu/2^{1/2}\sigma)]$, where μ and σ are the peak position and the width of the distribution, respectively. We set $\sigma = 1$ nm, a value motivated by the observed widths in the simulations. Using our experimentally determined value of $\langle E \rangle$ and eq 11, we solved eq 8 (with $l_c \to \infty$) to obtain μ, which we then used together with σ to calculate mean interdye distances as $\langle R \rangle = \int_0^{\infty} RP_{\mathrm{norm}}(R, \mu, \sigma)\,\mathrm{d}R$.

DOI: 10.1021/acs.jpcb.8b07537
J. Phys. Chem. B 2018, 122, 11626−11639

Finally, as an even rougher model, we considered the limit of a single fixed distance for the relatively stiff ssNA chains by inverting the Förster relation, $\langle E \rangle = [1 + (R_{fixed}/R_0)^6]^{-1}$, to obtain R_{fixed} in terms of $\langle E \rangle$.

Fluorescence Anisotropy Decay Measurements. Time-resolved FAD measurements of the donor fluorophore were performed on constructs singly labeled with Alexa 488, to avoid complications from the FRET process. The acceptor anisotropy was measured on doubly labeled constructs using direct acceptor excitation. The experimental conditions were: 150 mM NaCl, 0.001% Tween 20, 143 mM BME in 10 mM HEPES buffer (3.47 mM NaOH, pH 7.0) with a sample concentration of 50 nM. Measurements were performed on a custom-built ensemble fluorescence lifetime spectrometer[85] at 22 °C. The donor fluorophores were excited with the donor excitation source using a repetition rate of 20 MHz. The acceptor fluorophores were excited by the acceptor excitation source. The pulse frequency was adjusted to 20 MHz (Optical Supercontinuum Systems SC450−4, Fianium, Southampton, U.K.). The emitted donor fluorescence was filtered with an ET 525/50 filter and the acceptor fluorescence with an HQ 650/100 filter (both Chroma Technology). The emitted photons were detected with a microchannel plate photomultiplier tube (R3809U-50; Hamamatsu City, Japan), preamplified (PAM 102-M; PicoQuant, Berlin, Germany), and the arrival times were recorded by a PicoHarp 300 photon-counting module (PicoQuant, Berlin, Germany). The measured instrument response functions for both lasers had a width of 100 ps. The G-factor was calculated from the ratio of the fluorescence intensity after horizontal excitation and horizontal detection, I_{HH}, and the fluorescence intensity after horizontal excitation and vertical detection, I_{HV},

$$G = \frac{I_{HV}}{I_{HH}} \tag{12}$$

To calculate the anisotropy decay, the samples were excited with vertically polarized light (V), and the horizontally (H) and vertically polarized emission were measured separately on the same detector. The anisotropy decay $r(t)$ was calculated from the measured decays, $I_{VV}(t)$ and $I_{VH}(t)$, according to

$$r(t) = \frac{I_{VV}(t) - GI_{VH}(t)}{I_{VV}(t) + 2GI_{VH}(t)} \tag{13}$$

RESULTS

Dye Dynamics in Simulations of Covalently Attached Dyes. *Fluorophore Labeled Dinucleotides.* The dynamical and conformational behavior of the denovo parametrized dyes was tested first in simulations of either Alexa 594 or Alexa 488 dye-labeled thymine dinucleotides solvated with different water models (TIP3P,[54] TIP4P-Ew,[55] TIP4P/2005,[49] TIP4P/2005(1.1),[46,49] and TIP4P-D[48]). The rotational analysis was performed in a DNA-fixed reference frame by superposition of the dinucleotide, thereby removing the tumbling of the DNA. From the resulting trajectories, we calculated the correlation functions $r_I(t)$ of the unit vectors of the transition dipoles $\hat{\boldsymbol{\mu}}$ of the dyes in a reference frame defined by the nucleobases (Figure 2A,C).

The order parameters S^2 and S_f^2, as obtained by fits of eq 6 to the $r_I(t)$ calculated from MD trajectories, follow a common trend with respect to the different water models. For both dyes, S_f^2 is smallest for TIP4P-D, followed by TIP4P/2005 ~ TIP4P/2005(1.1) < TIP3P < TIP4P-Ew (where TIP4P/2005 leads to a smaller S_f^2 for Alexa 594 and TIP4P/2005(1.1) to a smaller value for Alexa 488) (Table 1). S^2 values are ordered as

Table 1. Fitting Parameters of the Decay of the MD Anisotropy Decay for Dyes Alexa 594 and Alexa 488 Attached to dT_2 According to Equation 6

water model	S_f^2	τ_f [ns]	τ_s [ns]	S^2
	Alexa 594			
TIP3P[54]	0.80	0.17	16.93	0.58
TIP4P-Ew[55]	0.89	0.06	2.60	0.75
TIP4P/2005[49]	0.62	0.31	59.22	0.04
TIP4P/2005(1.1)[46,49]	0.74	0.16	29.74	0.63
TIP4P-D[48]	0.40	0.28	5.36	0.25
	Alexa 488			
TIP3P[54]	0.57	0.13	9.93	0.13
TIP4P-Ew[55]	0.67	0.14	7.09	0.37
TIP4P/2005[49]	0.56	0.19	11.89	0.18
TIP4P/2005(1.1)[46,49]	0.48	0.23	11.87	0.15
TIP4P-D[48]	0.28	0.23	9.32	0.05

TIP4P-D < TIP3P < TIP4P/2005(1.1) < TIP4P/2005 < TIP4P-Ew for Alexa 488 and as TIP4P/2005 < TIP4P-D < TIP3P < TIP4P/2005(1.1) < TIP4P-Ew for Alexa 594. We assigned the two time scales of the $r_I(t)$ decay to a fast and relatively unrestricted motion of the dye, τ_f, and a slower motion influenced by stacking and unstacking of the dye to adjacent nucleobases, τ_s. respectively. For all water models, we found τ_f to be about 0.1 to 0.3 ns. τ_s is one to two orders of magnitude slower. From the FAD analysis, we conclude that the movement of the dyes is least restricted in simulations with TIP4P-D water.

To study the dynamics of the dyes in more detail, we tracked the distance between the geometric center of the central ring of each dye and the geometric center of its directly adjacent nucleobase (Figure 2B,D). Long periods of nearly constant distance indicate stacking to the proximal base (short distance) or the distal base (long distance). For most water models (TIP3P, TIP4P-Ew, TIP4P/2005, TIP4P/2005(1.1)), Alexa 594 remained nearly continuously stacked to one of the two nucleobases of the dinucleotides. For all water models sharp peaks dominate the dye-nucleotide distance distributions. Visual inspection of these segments of the trajectories reveal strong stacking of the dyes onto one of the two nucleobases or even intercalation between the bases. For Alexa 488, a similar trend is observed, although the smaller ring system does not stack quite as strongly onto the nucleobases. Nevertheless, for most water models one or two sharp peaks dominate the distance distributions.

By contrast, both dyes simulated in TIP4P-D water sample a broader spectrum of dye−nucleotide distances. The dispersion correction of this water model results in a more effective solvation of the dyes and alleviates the problem of over-abundant dye stacking to nucleobases. For further studies, we thus primarily used the TIP4P-D water model.[48] Moreover, we also tested the TIP4P/2005(1.1) water model further, as this approach had been found to account well for experimental FAD measurements on proteins.[36]

Fluorophores Attached to ssDNAs. To study the dynamics of fluorescent dyes attached to 19mer ssDNA, we simulated single-stranded dT_{19} and dA_{19} with both dyes covalently attached. From these trajectories, we calculated the time-

DOI: 10.1021/acs.jpcb.8b07537
J. Phys. Chem. B 2018, 122, 11626−11639

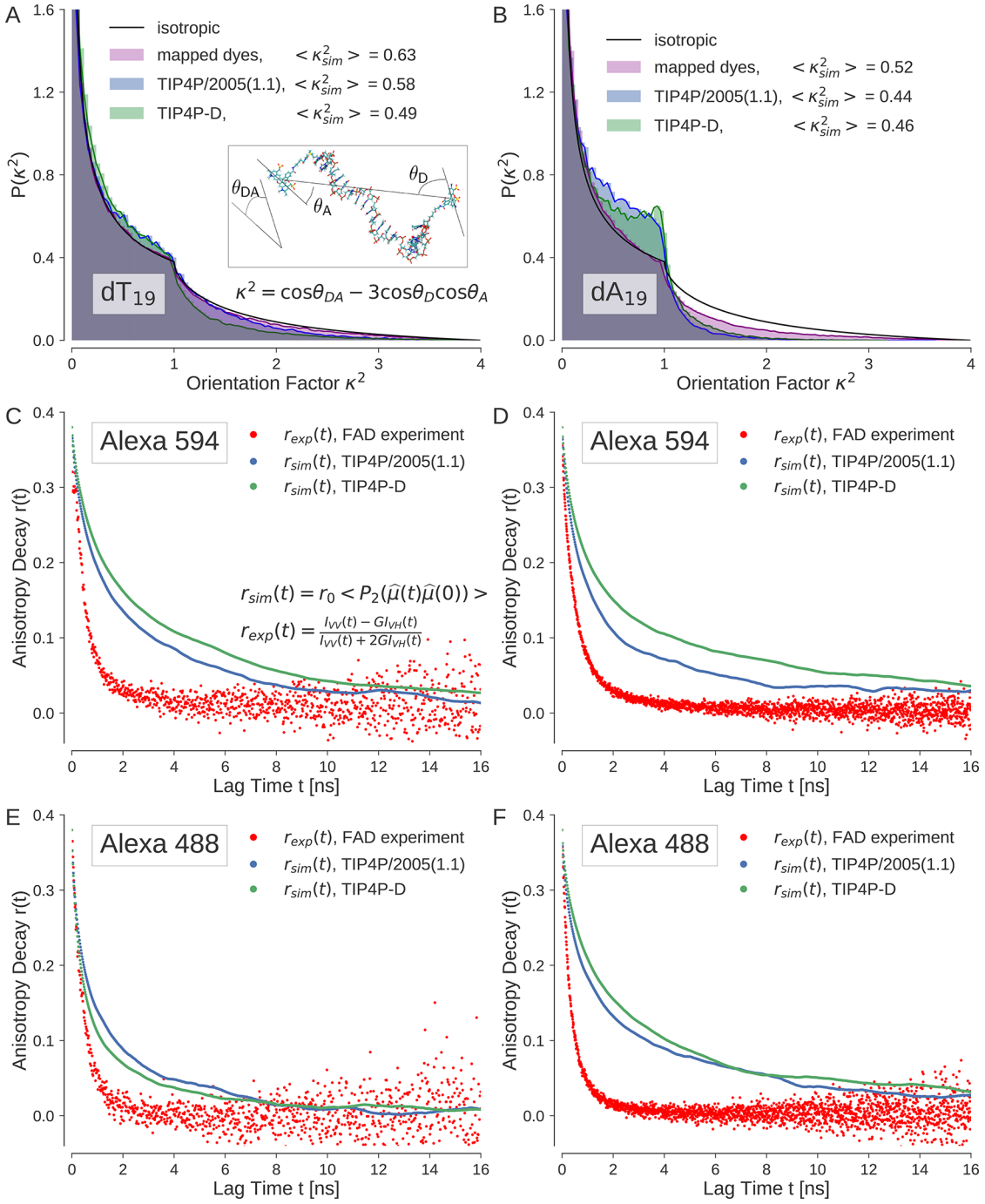

Figure 3. Orientation factor κ^2 of Alexa 594 and 488 covalently attached to ssDNA. (A, B) Distributions of κ^2 for dT_{19} (A) and dA_{19} (B). FAD calculated from simulations of fluorescent dyes Alexa 594 (C, D) and Alexa 488 (E, F) covalently attached to dT_{19} (C, E) and dA_{19} (D, F). Experimental FAD measurements are shown in red. The simulations were performed in TIP4P-D water[48] (green) and TIP4P/2005(1.1) water[46,49] (blue), respectively.

dependent orientation factor κ^2. We also related the dynamics in the simulations to the FAD measurements to validate the performance of the parametrization of the dyes for the two water models that we selected in the previous analysis, TIP4P/2005(1.1) and TIP4P-D.

Dye Orientation. Due to the structural composition of the systems, i.e., rod-like nucleic acids with dyes attached by flexible linkers to their ends, one would expect a nearly isotropic distribution of the dye orientations. The simulations with dyes attached to dT_{19} (Figure 3A) capture the theoretical distribution of an isotropically oriented label remarkably well (Figure 3A). The mean values of κ^2 are 0.58 (TIP4P/2005(1.1)) and 0.49 (TIP4P-D), and thus reasonably close to the isotropic mean of 2/3, which is typically assumed in the analysis of FRET measurements if the fluorescence anisotropies are low. The shift to smaller κ^2 values in the latter simulation is due to an intercalation of Alexa 594 within the last two terminal bases, which is presumably an artifact caused by a residual tendency for dye-base stacking. Nevertheless, for dT_{19} the orientation of the dyes seems to be described reasonably well using both water models.

DOI: 10.1021/acs.jpcb.8b07537
J. Phys. Chem. B 2018, 122, 11626−11639

The distribution of the orientational factor κ^2 of the dyes attached to dA_{19} is shifted to smaller values for both water models (Figure 3B), with mean values of 0.44 (TIP4P/2005(1.1)) and 0.46 (TIP4P-D), respectively. From the trajectories, it is apparent that the terminal bases of dA_{19} tend to interact more strongly with the dyes.

Comparison of Dye Dynamics to Experiment. The dynamics of the dyes attached to the nucleic acids can be compared to FAD measurements by computing the autocorrelation function $r(t)$ (eq 5) reporting on FAD (eq 13). The calculated FAD curves for Alexa 488 attached to dT_{19} in TIP4P-D and TIP4P/2005(1.1) water match the experimental data reasonably well (Figure 3E). Nevertheless, in all cases the simulated orientational dynamics is too slow compared to FAD measurements (Figure 3C–F). This indicates that the dyes lose memory of their orientation well before 2 ns. We attribute the slow simulated decays to the Alexa dyes sticking too strongly to nucleobases, even with dispersion-corrected dye-water interactions.

The comparison of rotational correlation functions to FAD measurements, together with the analysis of the orientation factor κ^2, suggests that the orientation and conformational freedom of the dyes is described reasonably well for dT_{19} and also quite well for dA_{19}, but the dynamics of the dyes are still too slow because of overabundant stacking.

Fluorophore Mapping onto ssNAs. To circumvent the problem of dye stacking even with an improved description of the dye-water interaction, and to speed up the MD simulations by using smaller boxes, we implemented a dye-mapping approach. Every 0.2 ns, a random dye configuration from a simulation of fluorescently labeled dinucleotides was mapped onto the terminal nucleobases of long unlabeled ssNA simulation trajectories. The dye library was generated from the dinucleotide MD simulations using TIP4P-D (see Methods).

Dye Orientation. For all three ssNAs, dT_{19}, dA_{19}, and rA_{19}, the mapping approach captures the fully isotropic behavior expected for fluorophores attached to single-stranded nucleic acids (Figures 3A,B and 4A). The mapping approach leads to distributions of the orientation factor κ^2 comparable to isotropically oriented dyes. The mean values of κ^2 are 0.63 and 0.71 for dT_{19} and rA_{19}, respectively, close to the isotropic mean of $\kappa^2 = {}^2/_3$. For dA_{19}, the calculated mean value of 0.52 falls somewhat below the isotropic mean, but it is closer than in simulations with directly attached dyes. From the near-isotropic distributions obtained with dye mapping, we conclude that the underlying dye libraries contain sufficiently diverse dye conformations that provide good coverage of the configurational space.

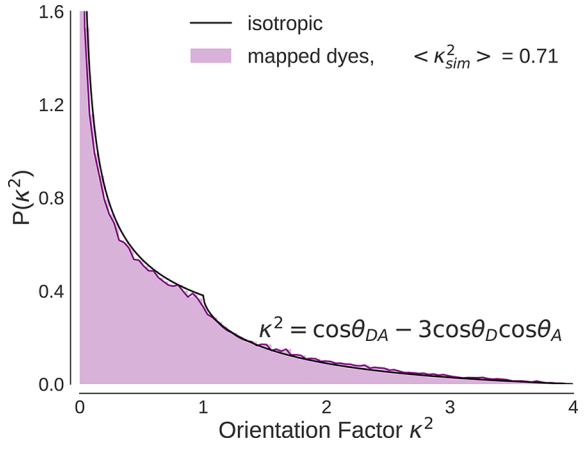

Figure 4. Orientation factor κ^2 of Alexa 594 and 488 dyes mapped onto single-stranded homopolymeric RNA, rA_{19}. Distribution of κ^2 from simulations (purple) and for an isotropic dye distribution (black).

FRET Efficiencies and Interdye Distances for ssDNA. *ssDNA Simulations with Covalently Attached Dyes.* We used the path integral formulation of Makarov and Plaxco[75] (eq 1) to calculate FRET efficiencies from the MD simulations. For ssDNA simulated with covalently attached dyes at 150 mM NaCl, the calculated FRET efficiencies are lower than in experiment. Correspondingly, the interdye distances $R_{dye-dye}$ are overestimated in simulations with dyes explicitly attached for both TIP4P-D and TIP4P/2005(1.1) (Figure 5). The underestimation of the efficiencies compared to experiment might be a result of insufficient sampling or overabundance of base–base stacking, which keeps the polymers in extended helical conformations. The simulations were initiated from helical configurations, and trajectories of less than 2 μs (TIP4P/2005(1.1)) and 2–4 μs (TIP4P-D) might have been too short to fully sample the relevant conformational space of the nucleic acids dT_{19} and dA_{19}. However, large boxes with about 230 000 atoms are required to simulate fully labeled ssDNA, which limits the accessible simulation time scales. By contrast, unlabeled ssDNA required boxes with only 65 000 atoms. In the following, we therefore explore an alternative route to studying different nucleic acids over a range of salt concentrations.

ssNA Simulations Analyzed with Dye Mapping. As a computationally efficient alternative to costly simulations with explicit dyes, we implemented a dye-mapping approach. We constructed libraries of dye conformers from the MD simulations of dye-labeled dinucleotides, and then mapped the dyes onto structures from simulations of unlabeled ssNAs. In this way, we could take advantage of the more efficient and exhaustive sampling of both the nucleic acid and dye conformational spaces. Multiple different dye conformations, randomly drawn from an equilibrium distribution of dye orientations, were mapped onto each simulation structure. By repeating this procedure, we constructed multiple trajectories of dye-labeled ssNAs from a single MD trajectory of an unlabeled molecule.

Without dyes, the simulation systems were substantially smaller, and we could simulate each ssDNA and ssRNA for 20 μs and 7 μs, respectively, at each of the three salt concentrations studied by MD simulation. However, because the ends were inaccessible in some configurations, we could not map dye conformers onto every single frame of the trajectory. This steric hindrance reduced the effective length of the ssDNA trajectories at high salt to 16 μs and 15 μs for dT_{19} and dA_{19}, respectively, and at intermediate salt concentration for dT_{19} to 16 μs. For ssRNA, the trajectory at high salt concentration after the mapping was reduced to a total time of 4 μs.

ssDNA. At low salt concentration, the backbone of dT_{19} remained almost fully extended (Figure 6). With only a few counterions in the simulation box, the charged phosphate groups of the backbone biased the nucleic acid toward extended, helical conformations. By contrast, at high salt concentration the backbone charges were screened, and collapsed backbone conformations dominated the ensemble.

DOI: 10.1021/acs.jpcb.8b07537
J. Phys. Chem. B 2018, 122, 11626–11639

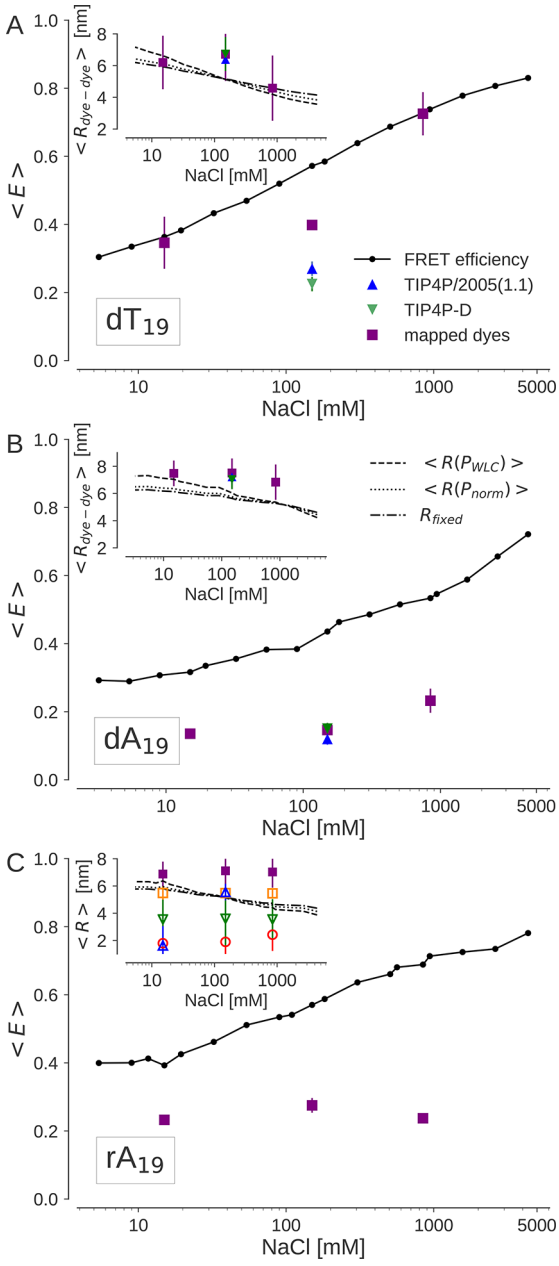

Figure 5. Mean FRET efficiencies of (A) dT_{19}, (B) dA_{19}, and (C) rA_{19}. MD results at low (15 mM), intermediate (150 mM), and high (845 mM) NaCl concentrations for mapped dyes are shown in purple, and for explicitly simulated dyes at 150 mM salt in green (TIP4P-D[48]) and blue (TIP4P/2005(1.1)[46,49]). Experiments are in black, with lines to guide the eye. The experimental transfer efficiencies are within an overall uncertainty of ±0.03. Insets in parts A and B show interdye distances $R_{dye-dye}$, with experimental values (lines) obtained for three different distance distributions (normal distribution, worm-like chain, and rod). The inset in part C shows the interdye distances $R_{dye-dye}$ (filled purple symbols) and the C5′−C3′ end-to-end distances (open symbols) for rA_{19} from DESRES simulations[44] (orange), and from parmBSC0χ_{OL3} simulations[58−60] with TIP3P[54] (red), TIP4P/2005(1.1)[46,49] (blue), and TIP4P-D[48] water (green). Error bars indicate standard errors of the mean transfer efficiencies (main plots) and standard deviations σ_R of the distances (insets), respectively.

Some of these structures were stabilized by hydrogen bonds mediating thymine−thymine interactions. The structures at intermediate salt concentration were in between the two

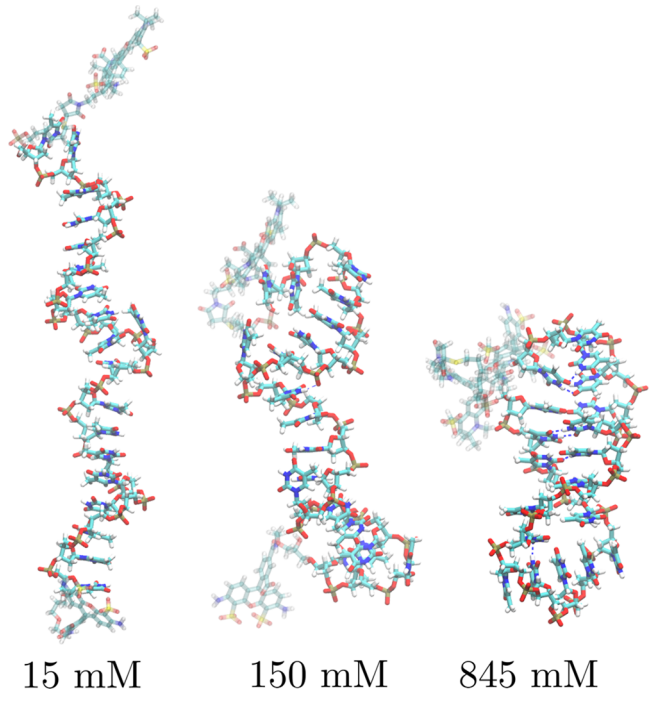

Figure 6. Representative structures of dT_{19} simulated with the parmBSC1 force field[38] in TIP3P water[54] at three salt concentrations. Mapped dyes are shown in transparent representation. Dashed lines represent H-bonds.

extremes observed at low and high salt concentrations. In general, at all three salt concentrations, diverse ensembles of different configurations were sampled, with standard deviations σ_R of 1.6, 1.7, and 2.1 nm for the interdye distances $R_{dye-dye}$ (at low, intermediate and high salt, respectively) (inset in Figure 5A). Visually (Figure 6), the dT_{19} chain at intermediate salt concentration appears as helical segments connected by nucleotides acting as flexible hinges. Hydrogen bonding locked these hinges into near-90° angles. Similar structures were also found in the simulations employing TIP4P/2005(1.1) and TIP4P/D water.

For dA_{19}, we did not observe a strong dependence of the structures on the salt concentration (Figures 5B and 7). However, σ_R increased with increasing salt concentration (0.9, 1.1, and 1.3 nm), indicating a broader distribution of interdye distance $R_{dye-dye}$ at high salt concentration. Visual inspection showed elongated conformations with nearly fully stacked bases for all three salt concentrations. The purine bases seemed to stack so strongly that screening of the charged backbone did not promote formation of compact conformations. Transiently, elongated helical conformations would separate into shorter segments. However, in contrast to dT_{19}, the bends in the backbone did not seem to be stabilized by hydrogen bonding, such that the bases would return to the elongated helical conformations within a few nanoseconds. Moreover, visually these bending motions of the backbone were sampled less frequently than for dT_{19}. Single bases transiently rotated out of the elongated conformations only to rotate back within a few nanoseconds. For dA_{19}, the salt-dependence of the apparent conformational landscape is subtle. As pointed out above, slightly longer end-to-end distances were sampled at low salt. However, the structures sampled in the simulations at different salt concentrations are visually similar to each other. In general, for dA_{19} the mean FRET efficiency was notably under-

DOI: 10.1021/acs.jpcb.8b07537
J. Phys. Chem. B 2018, 122, 11626−11639

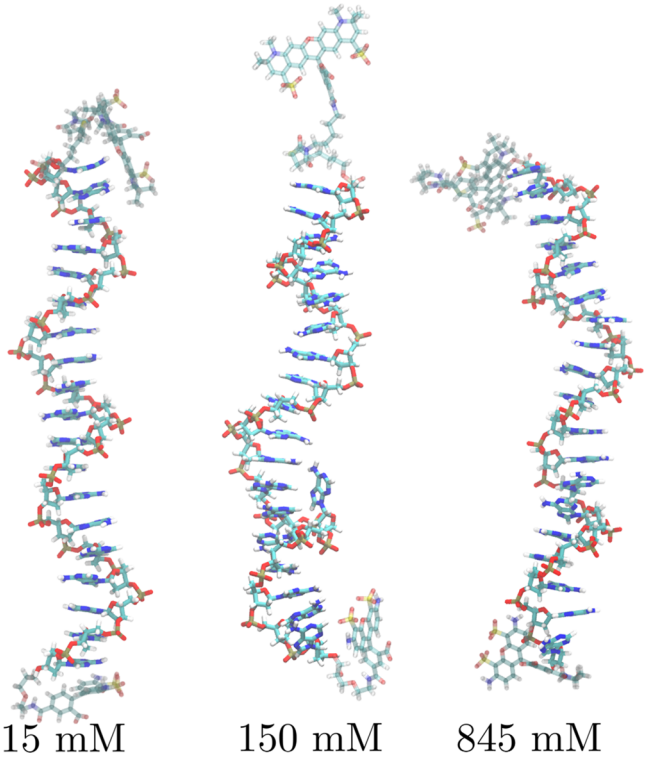

Figure 7. Representative structures of dA_{19} simulated with the parmBSC1 force field[38] in TIP3P water[54] at three salt concentrations. Mapped dyes are shown in transparent representation.

estimated at all salt concentrations (Figure 5B), presumably resulting from an over-representation of the highly extended structures. Analysis of selected frames indicates that the sugar is in C2′-endo puckering in all ssDNA structures.

For ssDNA, we found that parmBSC1[38] in combination with the computationally efficient TIP3P water model[54] captures the overall trend of experimental mean transfer efficiencies for homopolymeric dT_{19} and roughly describes the experimentally observed trend for homopolymeric dA_{19}. Additionally, we showed that our dye-mapping approach to calculate FRET efficiencies from MD simulations is viable.

ssRNA. Simulation of rA_{19} with the parmBSC0χ_{OL3} force field[58−60] solvated in TIP3P water[54] quickly led to a collapse of the initially helical structure at all salt concentrations (Figure 8). A similar collapse was reported for rU_{40} by Tan et al.[44] For rA_{19}, the calculated C5′-C3′ end-to-end distances (inset of Figure 5C) dramatically underestimate the experimental interdye distances. In the collapsed structures, we even observed intercalations of nucleobases (bottom left of 15 mM structure in (Figure 8). To improve the solvation of the ssRNA, simulations of rA_{19} solvated in TIP4P/2005(1.1)[46,49] and TIP4P-D water[48] were performed. Although TIP4P/2005(1.1)[46,49] improved the comparison to experimental data at intermediate salt concentration (blue) and TIP4P-D[48] at all salt concentrations (green), the mean end-to-end distances remained too short. The structures sampled with these two water models were still too collapsed, with a loss of helical twist and intercalated bases, and in some cases, the initially helical structure was bent into ring-like shapes (Figure 8).

The recently developed DESRES force field[44] improved the description of the mean C5′-C3′ end-to-end distances substantially (inset in Figure 5C). Nevertheless, the simulations of rA_{19} do not reproduce the experimentally

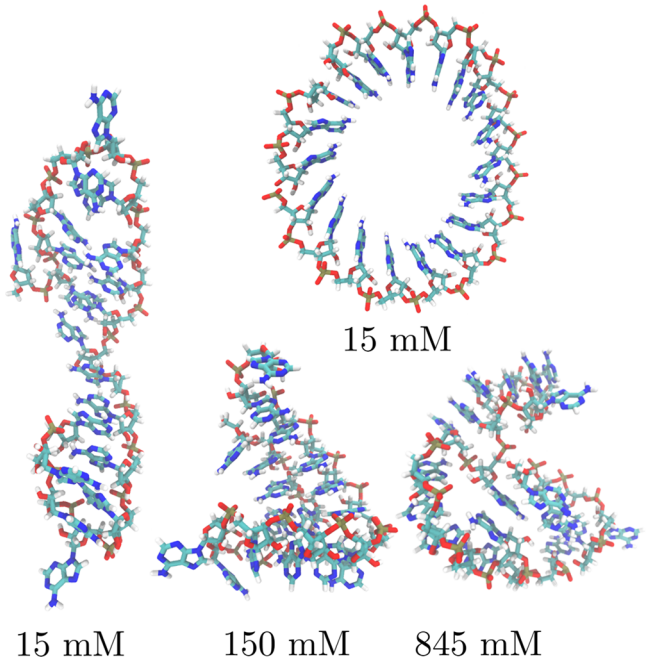

Figure 8. Representative structures of rA_{19} simulated with the parmBSC0χ_{OL3} force field[58−60] in TIP3P water.[54]

measured mean FRET efficiencies (Figure 5C). Visually, rA_{19} behaves similar to dA_{19}, remaining mostly extended (Figure 9)

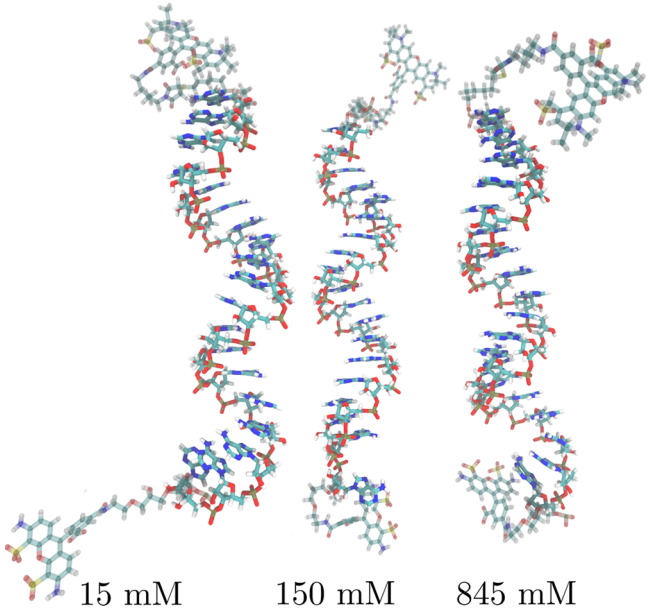

Figure 9. Representative structures of rA_{19} simulated with the DESRES force field[44] in TIP4P-D water.[48] Mapped dyes are shown in transparent representation.

with few short-lived bends of the backbone and single nucleotides transiently rotating out of the single-stranded helix. These disruptions of the helix do not appear to depend significantly on the salt concentration, in contrast to what Tan et al.[44] found in long trajectories of single-stranded rU_{40} in a range of 50 to 400 mM NaCl. For rA_{19}, the simulations capture the experimental $R_{dye-dye}$ distances at low NaCl concentrations (<100 mM), but for higher NaCl concentrations (>100 mM)

DOI: 10.1021/acs.jpcb.8b07537
J. Phys. Chem. B 2018, 122, 11626−11639

the $R_{dye-dye}$ distances sampled in our simulations (purple in the inset of Figure 5C) are larger than the distances deduced from experiment. In contrast, Tan et al.[44] obtained substantially lower end-to-end distances for rU_{40} in this salt regime. Homopolymeric pyrimidines are quite flexible, both as ssDNA and ssRNA. By comparison, the homopolymeric purine chain rA_{19} here largely retained the helical structure ($\sigma_R \approx 1$ nm irrespective of salt). The resulting configurations of rA_{19} are extended, and lead to an underestimation of the transfer efficiencies (Figure 5C). The failure to reproduce the experimental salt-dependence could mean that the DESRES force field overemphasizes the purine−purine stacking or that it is biased toward conformations resembling A-form helices.[42] Another concern is that our MD simulations may not have been long enough to sample the relevant configuration space. Overall, the DESRES force field[44] improves the quality of the description of single-stranded RNA, but substantial discrepancies between simulations and experiments remain.

Interdye Distances from FRET Measurements. The deviations we obtained in converting the FRET measurements back to interdye distances highlight the importance of choosing an adequate model for the distance distribution. Two crude models, a truncated normal distribution P_{norm} and a single fixed distance R_{fixed}, produce reasonable agreement with the mean efficiencies from simulation, even though they are unlikely to be realistic. The more elaborate worm-like chain distribution P_{WLC} seems to capture the simulated mean distance for low ionic strengths also for the purine chains (Figure 5B,C), even though for the mean efficiencies we see clear deviations.

DISCUSSION

Mapping the conformational space and dynamics of single-stranded nucleic acids is a problem of considerable importance due to their fundamental role in biological processes and their widespread applications in molecular medicine and nanotechnology. By performing all-atom MD simulations with explicitly included fluorescent dyes, we were able to test the quality of current computer models both for nucleic acids and for fluorescent dyes, which makes it possible to begin interpreting single-molecule FRET data in atomistic detail.

Dye Modeling. We first established that the dispersion correction of the TIP4P-D[48] and TIP4P/2005(1.1)[46,49] water models increases the solvation of the dyes and alleviates the stacking of the dyes to ssNAs. The distributions of the FRET orientation factor κ^2 obtained in simulations of ssNAs with explicit dyes were reasonably close to the expected isotropic distribution. However, the comparison to FAD measurements showed that the dynamics of the dyes in the simulations remained too slow, suggesting overly strong stacking between the dyes and both pyrimidines and purines even in dispersion-corrected water. Moreover, calculating the FRET efficiencies from simulations with dyes explicitly attached to ssNAs is challenging due to the computational cost of generating long trajectories for the dye-linker-ssNA systems (here with 230 000 atoms).

Mapping dyes onto structures from simulations of unlabeled ssNA, which are computationally more tractable (here requiring only 65 000 atoms), provided a way forward to compare MD simulations with single-molecule FRET. Experimentally, the dye orientation relaxes on a ∼1 ns time scale (Figure 3C−F), much faster than the end-to-end distance relaxation time of the nucleic acids, which motivates the use of dye rotamer libraries similar to those used in protein simulations.[32,33,74] Here we constructed dye rotamer libraries for nucleic acids from simulations of explicit dyes attached to dinucleotides solvated in TIP4P-D water model.[48] These simulations produced dye conformations at atomic resolution, which we could then map onto the ssNAs. Mapping of dyes onto label-free ssNAs greatly improved the dye orientational sampling and reduced the problem of dye stacking. Future improvement of the rotamer libraries via, e.g., enhanced sampling methods, might provide even more realistic distributions of dye conformations. In combination, dye mapping using dispersion-corrected dye rotamer libraries provides the basis for the efficient calculation of FRET efficiencies from MD simulations of nucleic acids. A better description of the dyes will enable quantitative comparisons and holds the promise to use fluorescence data for ensemble refinement[86] of nucleic acids.[43]

FRET Efficiencies vs Interdye Distances. In the literature, MD simulations are often compared to interdye or end-to-end distances deduced from single-molecule FRET or X-ray scattering experiments.[22,44,87] By calculating the mean distance between the dyes, $\langle R \rangle$, using the mean transfer efficiency, $\langle E \rangle$, we were able to show that obtaining matching interdye distances does not guarantee good agreement between experimental and simulated transfer efficiencies (Figure 5B). Some potential sources of this inconsistency are the assumptions associated with calculating a mean distance from measured mean transfer efficiencies. For dynamic, conformationally heterogeneous polymers, one requires knowledge about the distribution of interdye distances and the time scale on which they interconvert.[25] Although these properties have been well characterized for unfolded and intrinsically disordered proteins,[88] they remain poorly understood for unstructured ssNAs and merit further investigation. For these reasons, it is perhaps most practical to compare experimental and simulated transfer efficiencies, which highlights the importance of properly incorporating the fluorophores into state-of-the-art MD simulations.

Force Fields. The good consistency of simulations with explicit dyes and with mapped dyes, and the visual inspection of the ssDNA and ssRNA configurations suggest that the deviations between experimentally measured and simulated FRET efficiencies are due primarily to remaining issues in the nucleic acid force fields. In this regard, ssRNA remains particularly challenging. The parmBSC0χ_{OL3}[58−60] force field for RNA in combination with TIP3P water[54] was found to favor collapsed purine chains, a behavior reported also for single-stranded pyrimidine chains.[44] Solvation of the system in different water models (TIP4P/2005(1.1)[46,49] and TIP4P-D[48]) marginally improved the conformational ensemble. The recently developed DESRES[44] force field prevented this purine-chain collapse, at least on the time scales studied. However, the comparison to single-molecule FRET data indicates that helical structures may be too persistent, which may stem from an overestimate of purine−purine stacking or from overly stabilizing helices.[42] It will also be important to further test the DESRES force field in simulations of folded structures, which are typically described well by the parmBSC0χ_{OL3} force field.[12] The development of balanced force fields that describe unfolded and folded RNAs well remains challenging.

Nevertheless, our results indicate significant progress toward meaningful comparisons of FRET values from experiment and

DOI: 10.1021/acs.jpcb.8b07537
J. Phys. Chem. B 2018, 122, 11626−11639

theory. We could show that the purine systems of both ssRNA and ssDNA are described reasonably with the force fields DESRES[44] and parmBSC1,[38] respectively. Both systems underestimate the measured FRET efficiencies, suggesting that compact structures are underrepresented in both configurational ensembles. Moreover, we could show that a state-of-the-art force field for DNA, parmBSC1,[38] matches the experimentally observed salt dependence of the homopolymeric pyrimidine chain dT_{19} remarkably well. This finding highlights both that current DNA force fields[37,38] can capture salient features of unfolded DNA and that dye mapping is a viable and efficient approach for getting transfer efficiencies from MD simulations of unlabeled nucleic acids.

CONCLUDING REMARKS

We showed that the dispersion correction in TIP4P-D[48] and TIP4P/2005(1.1)[46,49] water alleviates the problem of extensive dye-base stacking in fluorophore-labeled nucleic acids. Simulations of dye-labeled nucleic-acid fragments with dispersion-corrected water models allowed us to create dye rotamer libraries. We used these libraries in a dye-mapping approach to calculate FRET efficiencies for long, end-labeled ssDNA and ssRNA at low, intermediate, and high salt concentrations. This mapping approach not only speeds up the FRET calculation but also removes some of the deficiencies seen in simulations of nucleic acids with explicit dye labels. From detailed comparisons to FAD and single-molecule FRET experiments, we conclude that the state-of-the-art force fields parmBSC1[38] and DESRES[44] describe single-stranded DNA and RNA in a reasonable manner.

ASSOCIATED CONTENT

Supporting Information

The Supporting Information is available free of charge on the ACS Publications website at DOI: 10.1021/acs.jpcb.8b07537.

Tables and figures listing the partial charges of the fuorescent dyes Alexa 488 and Alexa 594 and of their thiol linkers and a figure showing single-molecule FRET efficiency histograms (PDF)

AUTHOR INFORMATION

Corresponding Authors

*(B.S.) E-mail: schuler@bioc.uzh.ch.

*(G.H.) E-mail: gerhard.hummer@biophys.mpg.de.

ORCID

Lukas S. Stelzl: 0000-0002-5348-0277

Benjamin Schuler: 0000-0002-5970-4251

Gerhard Hummer: 0000-0001-7768-746X

Notes

The authors declare no competing financial interest.

ACKNOWLEDGMENTS

We thank Daniel Nettels for help with instrumentation and data analysis tools and Martin Vögele for help with the dye parametrization. K.K.G., M.H., L.S.S, and G.H. acknowledge financial support by the German Research Foundation (CRC 902: Molecular Principles of RNA Based Regulation) and the Max Planck Society. M.F.N., E.D.H., and B.S. acknowledge financial support by the Swiss National Science Foundation.

REFERENCES

(1) Chen, Z.; Yang, H.; Pavletich, N. P. Mechanism of Homologous Rrecombination from the RecA-ssDNA/dsDNA Structures. *Nature* **2008**, *453*, 489−494.

(2) Dickey, T. H.; Wuttke, D. S. The Telomeric Protein Pot1 from Schizosaccharomyces Pombe Binds ssDNA in Two Modes With Differing 3′ End Availability. *Nucleic Acids Res.* **2014**, *42*, 9656−9665.

(3) Wilson, K. S.; von Hippel, P. H. Transcription Termination at Intrinsic Terminators: The Role of the RNA Hairpin. *Proc. Natl. Acad. Sci. U. S. A.* **1995**, *92*, 8793−8797.

(4) Breaker, R. R. Riboswitches and the RNA World. *Cold Spring Harbor Perspect. Biol.* **2012**, *4*, a003566.

(5) Clark, D. P. *Molecular Biology: Understanding the Genetic Revolution*; Elsevier Science, 2009.

(6) Lange, H.; Sement, F. M.; Canaday, J.; Gagliardi, D. Polyadenylation-Assisted RNA Degradation Processes in Plants. *Trends Plant Sci.* **2009**, *14*, 497−504.

(7) Ku, T.-H.; Zhang, T.; Luo, H.; Yen, T. M.; Chen, P.-W.; Han, Y.; Lo, Y.-H. Nucleic Acid Aptamers: An Emerging Tool for Biotechnology and Biomedical Sensing. *Sensors* **2015**, *15*, 16281−16313.

(8) Bonauer, A.; Carmona, G.; Iwasaki, M.; Mione, M.; Koyanagi, M.; Fischer, A.; Burchfield, J.; Fox, H.; Doebele, C.; Ohtani, K.; et al. MicroRNA-92a Controls Angiogenesis and Functional Recovery of Ischemic Tissues in Mice. *Science* **2009**, *324*, 1710−1713.

(9) Plumridge, A.; Meisburger, S. P.; Pollack, L. Visualizing Single-Stranded Nucleic Acids in Solution. *Nucleic Acids Res.* **2017**, *45*, e66.

(10) Plumridge, A.; Meisburger, S. P.; Andresen, K.; Pollack, L. The Impact of Base Stacking on the Conformations and Electrostatics of Single-Stranded DNA. *Nucleic Acids Res.* **2017**, *45*, 3932−3943.

(11) Eichhorn, C. D.; Feng, J.; Suddala, K. C.; Walter, N. G.; Brooks, C. L., III; Al-Hashimi, H. M. Unraveling the Structural Complexity in a Single-Stranded RNA Tail: Implications for Efficient Ligand Binding in the Prequeuosine Riboswitch. *Nucleic Acids Res.* **2012**, *40*, 1345−1355.

(12) Šponer, J.; Bussi, G.; Krepl, M.; Banáš, P.; Bottaro, S.; Cunha, R. A.; Gil-Ley, A.; Pinamonti, G.; Poblete, S.; Jurečka, P.; et al. RNA Structural Dynamics as Captured by Molecular Simulations: A Comprehensive Overview. *Chem. Rev.* **2018**, *118*, 4177−4338.

(13) Ke, C.; Humeniuk, M.; S-Gracz, H.; Marszalek, P. E. Direct Measurements of Base Stacking Interactions in DNA by Single-Molecule Atomic-Force Spectroscopy. *Phys. Rev. Lett.* **2007**, *99*, 018302.

(14) Toan, N. M.; Thirumalai, D. On the Origin of the Unusual Behavior in the Stretching of Single-Stranded DNA. *J. Chem. Phys.* **2012**, *136*, 235103.

(15) Chen, H.; Meisburger, S. P.; Pabit, S. A.; Sutton, J. L.; Webb, W. W.; Pollack, L. Ionic Strength-Dependent Persistence Lengths of Single-Stranded RNA and DNA. *Proc. Natl. Acad. Sci. U. S. A.* **2012**, *109*, 799−804.

(16) Isaksson, J.; Acharya, S.; Barman, J.; Cheruku, P.; Chattopadhyaya, J. Single-Stranded Adenine-Rich DNA and RNA Retain Structural Characteristics of Their Respective Double-Stranded Conformations and Show Directional Differences in Stacking Pattern. *Biochemistry* **2004**, *43*, 15996−16010.

(17) Condon, D. E.; Kennedy, S. D.; Mort, B. C.; Kierzek, R.; Yildirim, I.; Turner, D. H. Stacking in RNA: NMR of Four Tetramers Benchmark Molecular Dynamics. *J. Chem. Theory Comput.* **2015**, *11*, 2729−2742.

(18) Reining, A.; Nozinovic, S.; Schlepckow, K.; Buhr, F.; Fürtig, B.; Schwalbe, H. Three-State Mechanism Couples Ligand and Temperature Sensing in Riboswitches. *Nature* **2013**, *499*, 355−359.

(19) Wacker, A.; Buck, J.; Mathieu, D.; Richter, C.; Wöhnert, J.; Schwalbe, H. Structure and Dynamics of the Deoxyguanosine-Sensing Riboswitch Studied by NMR-Spectroscopy. *Nucleic Acids Res.* **2011**, *39*, 6802−6812.

(20) Fürtig, B.; Richter, C.; Wöhnert, J.; Schwalbe, H. NMR Spectroscopy of RNA. *ChemBioChem* **2003**, *4*, 936−962.

DOI: 10.1021/acs.jpcb.8b07537
J. Phys. Chem. B 2018, 122, 11626−11639

(21) Murphy, M.; Rasnik, I.; Cheng, W.; Lohman, T. M.; Ha, T. Probing Single-Stranded DNA Conformational Flexibility Using Fluorescence Spectroscopy. *Biophys. J.* **2004**, *86*, 2530−2537.
(22) Zheng, W.; Borgia, A.; Buholzer, K.; Grishaev, A.; Schuler, B.; Best, R. B. Probing the Action of Chemical Denaturant on an Intrinsically Disordered Protein by Simulation and Experiment. *J. Am. Chem. Soc.* **2016**, *138*, 11702−11713.
(23) Stryer, L.; Haugland, R. P. Energy Transfer: A Spectroscopic Ruler. *Proc. Natl. Acad. Sci. U. S. A.* **1967**, *58*, 719−726.
(24) Schuler, B.; Eaton, W. A. Protein Folding Studied by Single-Molecule FRET. *Curr. Opin. Struct. Biol.* **2008**, *18*, 16−26.
(25) Schuler, B. Single-Molecule FRET of Protein Structure and Dynamics - A Primer. *J. Nanobiotechnol.* **2013**, *11*, S2.
(26) Haran, G. Single-Molecule Fluorescence Spectroscopy of Biomolecular Folding. *J. Phys.: Condens. Matter* **2003**, *15*, R1291−R1317.
(27) Truex, K.; Chung, H. S.; Louis, J. M.; Eaton, W. A. Testing Landscape Theory for Biomolecular Processes With Single Molecule Fluorescence Spectroscopy. *Phys. Rev. Lett.* **2015**, *115*, 018101.
(28) Best, R. B.; Merchant, K. A.; Gopich, I. V.; Schuler, B.; Bax, A.; Eaton, W. A. Effect of Flexibility and cis Residues in Single-Molecule FRET Studies of Polyproline. *Proc. Natl. Acad. Sci. U. S. A.* **2007**, *104*, 18964−18969.
(29) Merchant, K. A.; Best, R. B.; Louis, J. M.; Gopich, I. V.; Eaton, W. A. Characterizing the Unfolded States of Proteins Using Single-Molecule FRET Spectroscopy and Molecular Simulations. *Proc. Natl. Acad. Sci. U. S. A.* **2007**, *104*, 1528−1533.
(30) Wozniak, A. K.; Schröder, G. F.; Grubmüller, H.; Seidel, C. A. M.; Oesterhelt, F. Single-Molecule FRET Measures Bends and Kinks in DNA. *Proc. Natl. Acad. Sci. U. S. A.* **2008**, *105*, 18337−18342.
(31) Hoefling, M.; Lima, N.; Hänni, D.; Seidel, C. A. M.; Schuler, B.; Grubmüller, H. Structural Heterogeneity and Quantitative FRET Efficiency Distributions of Polyprolines Through a Hybrid Atomistic Simulation and Monte Carlo Approach. *PLoS One* **2011**, *6*, e19791.
(32) Boura, E.; Rozycki, B.; Herrick, D. Z.; Chung, H. S.; Vecer, J.; Eaton, W. A.; Cafiso, D. S.; Hummer, G.; Hurley, J. H. Solution Structure of the ESCRT-I Complex by Small-Angle X-Ray Scattering, EPR, and FRET Spectroscopy. *Proc. Natl. Acad. Sci. U. S. A.* **2011**, *108*, 9437−9442.
(33) Boura, E.; Rozycki, B.; Chung, H. S.; Herrick, D. Z.; Canagarajah, B.; Cafiso, D. S.; Eaton, W. A.; Hummer, G.; Hurley, J. H. Solution Structure of the ESCRT-I and II Supercomplex. Implications for Membrane Budding and Scission. *Structure* **2012**, *20*, 874−886.
(34) Kalinin, S.; Peulen, T.; Sindbert, S.; Rothwell, P. J.; Berger, S.; Restle, T.; Goody, R. S.; Gohlke, H.; Seidel, C. A. M. A Toolkit and Benchmark Study for FRET-Restrained High-Precision Structural Modeling. *Nat. Methods* **2012**, *9*, 1218−1225.
(35) Hoefling, M.; Grubmüller, H. In Silico FRET from Simulated Dye Dynamics. *Comput. Phys. Commun.* **2013**, *184*, 841−852.
(36) Best, R. B.; Hofmann, H.; Nettels, D.; Schuler, B. Quantitative Interpretation of FRET Experiments via Molecular Simulation: Force Field and Validation. *Biophys. J.* **2015**, *108*, 2721−2731.
(37) Zgarbová, M.; Šponer, J.; Otyepka, M.; Cheatham, T. E. I.; Galindo-Murillo, R.; Jurečka, P. Refinement of the Sugar-Phosphate Backbone Torsion Beta for AMBER Force Fields Improves the Description of Z- and B-DNA. *J. Chem. Theory Comput.* **2015**, *11*, 5723−5736.
(38) Ivani, I.; Dans, P. D.; Noy, A.; Pérez, A.; Faustino, I.; Hospital, A.; Walther, J.; Andrio, P.; Goñi, R.; Balaceanu, A.; et al. ParmBSC1: A Refined Force Field for DNA Simulations. *Nat. Methods* **2016**, *13*, 55−58.
(39) Stelzl, L. S.; Erlenbach, N.; Heinz, M.; Prisner, T. F.; Hummer, G. Resolving the Conformational Dynamics of DNA with Ångstrom Resolution by Pulsed Electron-Electron Double Resonance and Molecular Dynamics. *J. Am. Chem. Soc.* **2017**, *139*, 11674−11677.
(40) Dans, P. D.; Ivani, I.; Hospital, A.; Portella, G.; González, C.; Orozco, M. How Accurate are Accurate Force-Fields for B-DNA? *Nucleic Acids Res.* **2017**, *45*, 4217−4230.
(41) Galindo-Murillo, R.; Robertson, J. C.; Zgarbová, M.; Šponer, J.; Otyepka, M.; Jurečka, P.; Cheatham, T. E. Assessing the Current State of Amber Force Field Modifications for DNA. *J. Chem. Theory Comput.* **2016**, *12*, 4114−4127.
(42) Kührová, P.; Mlýnský, V.; Zgarbová, M.; Krepl, M.; Bussi, G.; Best, R. B.; Otyepka, M.; Šponer, J.; Banáš, P.; Improving the Performance of the RNA Amber Force Field by Tuning the Hydrogen-Bonding Interactions *bioRxiv* 2018.
(43) Bottaro, S.; Bussi, G.; Kennedy, S. D.; Turner, D. H.; Lindorff-Larsen, K. Conformational Ensembles of RNA Oligonucleotides from Integrating NMR and Molecular Simulations. *Science Adv.* **2018**, *4*, eaar8521.
(44) Tan, D.; Piana, S.; Dirks, R. M.; Shaw, D. E. RNA Force Field with Accuracy Comparable to State-of-the-Art Protein Force Fields. *Proc. Natl. Acad. Sci. U. S. A.* **2018**, *115*, E1346.
(45) Schröder, G. F.; Alexiev, U.; Grubmüller, H. Simulation of Fluorescence Anisotropy Experiments: Probing Protein Dynamics. *Biophys. J.* **2005**, *89*, 3757−3770.
(46) Best, R. B.; Zheng, W.; Mittal, J. Balanced Protein-Water Interactions Improve Properties of Disordered Proteins and Non-Specific Protein Association. *J. Chem. Theory Comput.* **2014**, *10*, 5113−5124.
(47) Norman, D. G.; Grainger, R. J.; Uhrín, D.; Lilley, D. M. J. Location of Cyanine-3 on Double-Stranded DNA: Importance for Fluorescence Resonance Energy Transfer Studies. *Biochemistry* **2000**, *39*, 6317−6324.
(48) Piana, S.; Donchev, A. G.; Robustelli, P.; Shaw, D. E. Water Dispersion Interactions Strongly Influence Simulated Structural Properties of Disordered Protein States. *J. Phys. Chem. B* **2015**, *119*, 5113−5123.
(49) Abascal, J. L. F.; Vega, C. A General Purpose Model for the Condensed Phases of Water: TIP4P/2005. *J. Chem. Phys.* **2005**, *123*, 234505.
(50) Corry, B.; Jayatilaka, D. Simulation of Structure, Orientation, and Energy Transfer between AlexaFluor Molecules Attached to MscL. *Biophys. J.* **2008**, *95*, 2711.
(51) Wang, J.; Wang, W.; Kollman, P. A.; Case, D. A. Automatic Atom Type and Bond Type Perception in Molecular Mechanical Calculations. *J. Mol. Graphics Modell.* **2006**, *25*, 247−260.
(52) Wang, J.; Wolf, R. M.; Caldwell, J. W.; Kollman, P. A.; Case, D. A. Development and Testing of a General AMBER Force Field. *J. Comput. Chem.* **2004**, *25*, 1157−1174.
(53) Vögele, M.; Köfinger, J.; Hummer, G. Molecular Dynamics Simulation of Carbon Nanotube Porins in Lipid Bilayers. *Faraday Discuss.* **2018**, *209*, 341−358.
(54) Jorgensen, W. L.; Chandrasekhar, J.; Madura, J. D.; et al. Comparison of Simple Potential Functions for Simulating Liquid Water. *J. Chem. Phys.* **1983**, *79*, 926−935.
(55) Horn, H. W.; Swope, W. C.; Pitera, J. W.; Madura, J. D.; Dick, T. J.; Hura, G. L.; Head-Gordon, T. Development of an Improved Four-Site Water Model for Biomolecular Simulations: TIP4P-Ew. *J. Chem. Phys.* **2004**, *120*, 9665−9678.
(56) Paschek, D.; Day, R.; García, A. E. Influence of Water-Protein Hydrogen Bonding on the Stability of Trp-cage Miniprotein. A Comparison Between the TIP3P and TIP4P-Ew Water Models. *Phys. Chem. Chem. Phys.* **2011**, *13*, 19840−19847.
(57) Salomon-Ferrer, R.; Case, D. A.; Walker, R. C. An Overview of the Amber Biomolecular Simulation Package. *WIRES Comput. Mol. Sci.* **2013**, *3*, 198−210.
(58) Pérez, A.; Marchán, I.; Svozil, D.; Šponer, J.; Cheatham, T. E., III; Laughton, C. A.; Orozco, M. Refinement of the AMBER Force Field for Nucleic Acids: Improving the Description of α γ Conformers. *Biophys. J.* **2007**, *92*, 3817−3829.
(59) Banáš, P.; Hollas, D.; Zgarbová, M.; Jurečka, P.; Orozco, M.; Cheatham, T. E.; Šponer, J.; Otyepka, M. Performance of Molecular Mechanics Force Fields for RNA Simulations: Stability of UUCG and GNRA Hairpins. *J. Chem. Theory Comput.* **2010**, *6*, 3836.
(60) Zgarbová, M.; Otyepka, M.; Šponer, J.; Mládek, A.; Banáš, P.; Cheatham, T. E.; Jurečka, P. Refinement of the Cornell et al. Nucleic

DOI: 10.1021/acs.jpcb.8b07537
J. Phys. Chem. B 2018, 122, 11626−11639

Acids Force Field Based on Reference Quantum Chemical Calculations of Glycosidic Torsion Profiles. *J. Chem. Theory Comput.* **2011**, *7*, 2886−2902.
(61) Joung, I. S.; Cheatham, T. E. Determination of Alkali and Halide Monovalent Ion Parameters for Use in Explicitly Solvated Biomolecular Simulations. *J. Phys. Chem. B* **2008**, *112*, 9020−9041.
(62) Hess, B.; Kutzner, C.; van der Spoel, D.; Lindahl, E. GROMACS 4: Algorithms for Highly Efficient Load-Balanced, and Scalable Molecular Simulation. *J. Chem. Theory Comput.* **2008**, *4*, 435−447.
(63) Sousa da Silva, A. W.; Vranken, W. F. ACPYPE - AnteChamber PYthon Parser interfacE. *BMC Res. Notes* **2012**, *5*, 367.
(64) Hess, B.; Bekker, H.; Berendsen, H. J. C.; Fraaije, J. G. E. M. LINCS: A Linear Constraint Solver for Molecular Simulations. *J. Comput. Chem.* **1997**, *18*, 1463−1472.
(65) Berendsen, H. J. C.; Postma, J. P. M.; van Gunsteren, W. F.; Di Nola, A.; Haak, J. R. Molecular Dynamics with Coupling to an External Bath. *J. Chem. Phys.* **1984**, *81*, 3684−3690.
(66) Bussi, G.; Donadio, D.; Parrinello, M. Canonical Sampling Through Velocity Rescaling. *J. Chem. Phys.* **2007**, *126*, 014101.
(67) Darden, T.; York, D.; Pedersen, L. Particle Mesh Ewald: An N log(N) Method for Ewald Sums in Large Systems. *J. Chem. Phys.* **1993**, *98*, 10089−10092.
(68) Parrinello, M.; Rahman, A. Polymorphic Transitions in Single Crystals: A New Molecular Dynamics Method. *J. Appl. Phys.* **1981**, *52*, 7182−7190.
(69) Michaud-Agrawal, N.; Denning, E. J.; Woolf, T. B.; Beckstein, O. MDAnalysis: A Toolkit for the Analysis of Molecular Dynamics Simulations. *J. Comput. Chem.* **2011**, *32*, 2319−2327.
(70) Gowers, R. J.; Linke, M.; Barnoud, J.; Reddy, T. J. E.; Melo, M. N.; Seyler, S. L.; Domański, J.; Dotson, D. L.; Buchoux, S.; Kenney, I. M.; Benthall, S.; Kenney, J. M.; Beckstein, O. MDAnalysis: A Python Package for the Rapid Analysis of Molecular Dynamics Simulations. *Proceedings of the 15th Python in Science Conference* **2016**, 98.
(71) McGibbon, R. T.; Beauchamp, K. A.; Harrigan, M. P.; Klein, C.; Swails, J. M.; Hernández, C. X.; Schwantes, C. R.; Wang, L.-P.; Lane, T. J.; Pande, V. S. MDTraj: A Modern Open Library for the Analysis of Molecular Dynamics Trajectories. *Biophys. J.* **2015**, *109*, 1528−1532.
(72) Humphrey, W.; Dalke, A.; Schulten, K. VMD − Visual Molecular Dynamics. *J. Mol. Graphics* **1996**, *14*, 33−38.
(73) Polyhach, Y.; Bordignon, E.; Jeschke, G. Rotamer Libraries of Spin Labelled Cysteines for Protein Studies. *Phys. Chem. Chem. Phys.* **2011**, *13*, 2356−2366.
(74) Warner, J. B.; Ruff, K. M.; Tan, P. S.; Lemke, E. A.; Pappu, R. V.; Lashuel, H. A. Monomeric Huntingtin Exon 1 Has Similar Overall Structural Features for Wild-Type and Pathological Polyglutamine Lengths. *J. Am. Chem. Soc.* **2017**, *139*, 14456−14469.
(75) Makarov, D. E.; Plaxco, K. W. Measuring Distances Within Unfolded Biopolymers Using Fluorescence Resonance Energy Transfer: The Effect of Polymer Chain Dynamics on the Observed Fluorescence Resonance Energy Transfer Efficiency. *J. Chem. Phys.* **2009**, *131*, 085105.
(76) Förster, T. Zwischenmolekulare Energiewanderung und Fluoreszenz. *Ann. Phys.* **1948**, *437*, 55−75.
(77) Hummer, G.; Szabo, A. Dynamics of the Orientational Factor in Fluorescence Resonance Energy Transfer. *J. Phys. Chem. B* **2017**, *121*, 3331−3339.
(78) Hillger, F.; Hänni, D.; Nettels, D.; Geister, S.; Grandin, M.; Textor, M.; Schuler, B. Probing Protein-Chaperone Interactions with Single-Molecule Fluorescence Spectroscopy. *Angew. Chem., Int. Ed.* **2008**, *47*, 6184−6188.
(79) Lipari, G.; Szabo, A. Model-Free Approach to the Interprettion of Nuclear Magnetic Resonance Relaxation in Macromolecules. 1. Theory and Range of Validy. *J. Am. Chem. Soc.* **1982**, *104*, 4546−4559.
(80) Clore, G. M.; Szabo, A.; Bax, A.; Kay, L. E.; Driscoll, P. C.; Gronenborn, A. M. Deviations from the Simple Two-Parameter Model-Free Approach to the Interpretation of Nitrogen-15 Nuclear Magnetic Relaxation of Proteins. *J. Am. Chem. Soc.* **1990**, *112*, 4989−4991.
(81) Lee, N. K.; Kapanidis, A. N.; Wang, Y.; Michalet, X.; Mukhopadhyay, J.; Ebright, R. H.; Weiss, S. Accurate FRET Measurements within Single Diffusing Biomolecules Using Alternating-Laser Excitation. *Biophys. J.* **2005**, *88*, 2939−2953.
(82) Kapanidis, A. N.; Lee, N. K.; Laurence, T. A.; Doose, S.; Margeat, E.; Weiss, S. Fluorescence-Aided Molecule Sorting: Analysis of Structure and Interactions by Alternating-Laser Excitation of Single Molecules. *Proc. Natl. Acad. Sci. U. S. A.* **2004**, *101*, 8936−8941.
(83) Hinczewski, M.; Netz, R. R. Dynamics of DNA: Experimental Controversies and Theoretical Insights. *Phys. A* **2010**, *389*, 2993−2996.
(84) O'Brien, E. P.; Morrison, G.; Brooks, B. R.; Thirumalai, D. How Accurate are Polymer Models in the Analysis of Förster Resonance Energy Transfer Experiments on Proteins? *J. Chem. Phys.* **2009**, *130*, 124903.
(85) Nettels, D.; Hoffmann, A.; Schuler, B. Unfolded Protein and Peptide Dynamics Investigated with Single-Molecule FRET and Correlation Spectroscopy from Picoseconds to Seconds. *J. Phys. Chem. B* **2008**, *112*, 6137−6146.
(86) Hummer, G.; Köfinger, J. Bayesian Ensemble Refinement by Replica Simulations and Reweighting. *J. Chem. Phys.* **2015**, *143*, 243150.
(87) Meisburger, S. P.; Sutton, J. L.; Chen, H. M.; Pabit, S. A.; Kirmizialtin, S.; Elber, R.; Pollack, L. Polyelectrolyte Properties of Single Stranded DNA Measured Using SAXS and Single-Molecule FRET Beyond the Wormlike Chain Model. *Biopolymers* **2013**, *99*, 1032−1045.
(88) Schuler, B.; Soranno, A.; Hofmann, H.; Nettels, D. Single-Molecule FRET Spectroscopy and the Polymer Physics of Unfolded and Intrinsically Disordered Proteins. *Annu. Rev. Biophys.* **2016**, *45*, 207−231.

DOI: 10.1021/acs.jpcb.8b07537
J. Phys. Chem. B 2018, 122, 11626−11639